The contents list available at the CBIORE journal website

International Journal of Renewable Energy Development

Journal homepage: https://ijred.cbiore.id

Research Article

Seawater utilization through hybrid photocatalysis-electrocoagulation process using pumice-supported g-C_3N_4/BiOBr for hydrogen production and methylene blue decolorization

Julius Rainer Sudianto[a], Reno Pratiwi[b], Bambang Heru Susanto[a], Slamet[a]*

[a]*Department of Chemical Engineering, Faculty of Engineering, Universitas Indonesia, Depok 16424, Indonesia*

[b]*Department of Petroleum Engineering, Faculty of Earth Technology and Energy, Universitas Trisakti, Jalan Kyai Tapa no.1, Jakarta 11440, Indonesia*

Abstract. This study investigated the simultaneous photocatalysis-electrocoagulation process using pumice-supported g-C_3N_4/BiOBr nanocomposites in seawater treatment to remove organic pollutants and generate hydrogen gas. The photocatalyst nanocomposite was synthesized via coprecipitation and immobilized on the pumice surface to enhance light exposure and facilitate catalyst recovery. The performance of the hybrid system was evaluated under various operational parameters, including applied voltage, seawater concentration, and pH. The results showed that the combined process outperformed the individual photocatalysis and electrocoagulation systems. Optimal performance was achieved at pH 3 and 15% seawater concentration, resulting in 99.37% methylene blue decolorization and 211 mL of hydrogen within 2 hours. At higher salinities and lower pH, increased coagulant formation caused a shadowing effect, limiting photocatalytic efficiency despite continued hydrogen evolution. The XPS (X-Ray Photoelectron Spectroscopy) characterization of the photocatalyst material, demonstrated the successful formation of a nanocomposite with a stable surface chemistry. Photoluminescence analysis confirmed that the charge separation mechanism could be enhanced, suppressing the recombination rate and being the primary reason for the enhanced photocatalysis process, although interfacial electronic interactions remained limited. Overall, this study demonstrates that the pumice-supported g-C_3N_4/BiOBr photocatalyst integrated with electrocoagulation provides an effective and stable platform for seawater-based hydrogen production and organic pollutant removal.

Keywords: Hydrogen, Photocatalysis, Electrocoagulation, Seawater, Renewable Energy

Received: 28th August 2025; Revised: 17th Dec 2025; Accepted: 8th January 2026; Available online: 1st February 2026

1. Introduction

The increasing demand for clean energy and the urgent need to mitigate climate change are driving the search for sustainable and resource-efficient renewable energy technologies. In this context, hydrogen has been recognized as a promising carrier in the world energy transition due to the high-energy content and lack of carbon emission throughout combustion (Cheekatamarla, 2024; Roy and Pramanik, 2024; L. Zhang *et al.*, 2024). Among the various hydrogen production methods, water splitting fueled by solar energy is considered one of the most attractive renewable energy sources (Badruzzaman et al., 2025; Imran and Hussain, 2024; Jia *et al.*, 2016). However, there is a scarcity of freshwater resources, which are often used in agriculture or for household purposes. This has led to a rise in the use of seawater as a rich and naturally conducting substance to produce hydrogen. Despite the abundant access to seawater, the large-scale use in green hydrogen infrastructure is still limited. This is due to the complexity of the ionic composition, as well as the inability to develop stable and effective catalysts operating in saline environments.

In this regard, solar and electrical energy can be used in a complementary pattern by relying on the hybrid processes of photocatalysis and electrochemical methods (Muttaqin *et al.*, 2022; Pratiwi *et al.*, 2025; Surjo *et al.*, 2024). Photocatalysis uses semiconductor materials to absorb light and produce electron-hole pairs for the production of redox reactions to split water and eliminate pollutants (Ali *et al.*, 2024; Hosseini *et al.*, 2023; R. Li and Li, 2017; Yusuf *et al.*, 2025). Meanwhile, electrocoagulation includes the application of direct current to sacrificial electrodes, made of aluminum/iron, which dissolves to create hydroxide flocs capturing dissolved contaminants (Al-Ajmi *et al.*, 2025; Boinpally *et al.*, 2023). These two systems are by-products of cathodic reduction to generate hydrogen gas, and the mechanisms of operation suggest a strong potential for synergistic interaction when implemented simultaneously.

Recent studies have shown that the combination of photocatalysis and electrocoagulation produces a significantly higher operational efficiency compared to the use of a single method (Muttaqin *et al.*, 2022; Pratiwi *et al.*, 2025; Surjo *et al.*, 2024). This enhanced performance is attributed to the interaction between these mechanisms. In terms of mechanisms of operation, the external electric field facilitates the extraction

* Corresponding author
Email: slamet@che.ui.ac.id (Slamet)

https://doi.org/10.61435/ijred.2026.61722
ISSN: 2252-4940/© 2026.The Author(s). Published by CBIORE

and acceleration of electrons produced in the photocatalyst by light. The process suppresses electron-hole recombination and promotes hydrogen evolution. Subsequently, organic contaminants and dyes are removed by coagulants formed during the electrocoagulation process, like aluminum hydroxide, increasing vulnerability to photocatalytic oxidation using the reactive oxygen species such as hydroxyl radicals. The light also experiences a local increase in the conductivity of the electrolyte due to the heat energy produced, which causes further reaction in electrochemical and photochemical processes.

A combination of photocatalysis-electrocoagulation processes has been applied in several studies using various objectives and catalysts. These include ciprofloxacin waste degradation and hydrogen production (Muttaqin *et al.*, 2022; Pratiwi *et al.*, 2022), COD removal of petroleum wastewater (Salman *et al.*, 2023), and the treatment of waste in the batik industry and hydrogen production (Pelawi *et al.*, 2020). Both electrolysis and photocatalytic processes have been reported for hydrogen production using seawater as a feedstock (Khan *et al.*, 2021; Zhang et al., 2024; Gupta et al., 2025). However, there is a limited report on the combination of electrocoagulation-based systems with photocatalytic processes operating concurrently to achieve simultaneous pollutant removal and hydrogen generation in high-salinity seawater environments. Specifically, photocatalysis and electrocoagulation of seawater with the g-C3N4/BiOBr composites with pumice support have attracted minimal attention. There is also limited information on the influence of salinity, pH, and coagulant formation on hydrogen evolution. The presence of salt ions in seawater can serve as electrolytes for electrocoagulation systems using ZnO/CuO-based electrodes (Harish *et al.*, 2017), and g-C_3N_4/BiOBr composites have been shown to effectively support photocatalytic activity (Tieng *et a*l., 2011). However, their integrated use, particularly g-C_3N_4/BiOBr immobilized on pumice, in a unified photocatalysis–electrocoagulation framework has not been reported.

In line with the knowledge gap, appropriate materials are selected in this study to ensure electrochemical stability and efficient coagulant generation under saline conditions. Specifically, stainless steel (SS316) and aluminum are used as the cathode and anode, respectively, due to their corrosion-resistant and electrochemically stable alloys. The sacrificial anode is made of aluminum, which has a high dissolution rate and capability to form Al3+ species at low-voltage conditions in comparison (Mechelhoff *et al.*, 2013). These ions hydrolyze to produce Al(OH)3 as a coagulant (removal of pollutants), which reacts with hydroxide ions (OH -) produced during the reduction of water by SS316, promoting the formation of floc.

Regarding the photocatalytic element, a composite of the graphitic carbon nitride (g-C3N4) and bismuth oxybromide (BiOBr) is prepared. Although g-C3N4 is characterized by the appropriate bandgap (=2.7 eV), good stability, and its ability to absorb visible light (Hayat *et al.*, 2022; Madankar *et al.*, 2025), it has poor performance because of the quick recombination of charges. To address this limitation, BiOBr, a layered, bismuth-based semiconductor with high resistance to photocorrosion and strong visible-light-driven activity, is coupled with g-C_3N_4 (Imam *et al.*, 2021; Meng *et al.*, 2021). The combination forms a Z-scheme heterojunction that allows the photogenerated electrons and holes to be spatially separated effectively, and the redox potential remains strong. This structure improves the production of the radicals of the hydroxyl and hydrogen required to degrade the pollutants and produce hydrogen simultaneously.

In order to enhance the light absorption and reuse of the catalysts, the composite is fixed on pumice stone. Pumice is selected because of a high level of porosity, chemical inertness, low-density, and floatability (Arenas *et al.*, 2025; Bonifaz Garcia, n.d.; Nazaruddin *et al.*, 2014). These characteristics enable the catalyst to stay suspended close to the solution surface, where photon flux is the highest, and in the process prevent sedimentation as well as secondary contamination. Moreover, pumice is porous, which also increases the catalyst loading, as well as offers alternative reaction spots.

Based on the material combination and system design, this study aims to evaluate the efficacy of an integrated photocatalysis-electrocoagulation system consisting of a g-C3N4/BiOBr composite immobilized on pumice to produce hydrogen and eliminate seawater pollutants. Major operational parameters such as applied voltage, seawater concentration, and pH are varied to optimize system performance, as assessed by pollutant degradation efficiency and hydrogen quantity. Furthermore, methylene blue is used as a model contaminant to represent different classes of organic pollutants in seawater. The results are expected to provide valuable information on how to create effective and sustainable technologies for seawater-based hydrogen generation.

2. Materials and Methods

2.1 Materials

Seawater was obtained from the coastal area in Muara Angke, Jakarta, Indonesia. The samples collected were stored at room temperature and filtered before use. Al and stainless steel 316 from the local market were used for the electrode. The synthesis process included melamine ($C_3H_6N_6$, Sigma-Aldrich), urea ($CO(NH_2)_2$, Sigma-Aldrich), ethanol (C_2H_6O, 99%, Sigma-Aldrich), bismuth (III) nitrate ($Bi(NO_3)_3.5H_2O$, Merck), acetic acid (CH_3COOH, 99%, Merck), sodium bromide (NaBr, Sigma-Aldrich), sodium acetate (CH_3COONa, Sigma-Aldrich), and tetraethyl orthosilicate ($SiC_8H_{20}O_4$, Sigma-Aldrich) to develop the g-C_3N_4/BiOBr. Distilled water functioned as a solvent. All chemicals were used as received without any further modifications or adjustments.

2.2 Synthesis of g-C_3N_4

The nanoparticles g-C_3N_4 were obtained by a two-stage calcination approach. Typically, 14.4 g of urea and 1.2 g of melamine were mixed into an alumina crucible with a cover in a muffle furnace at atmospheric conditions under the temperature increasing to 180$^{\circ C}$ with a heating rate of 2.5°C/min and held for 30 minutes. The second stage was followed by increasing the temperature to 500°C with the same heating rate and holding for 2 hours. Finally, the product was taken out of the muffle furnace and ground in a mortar to obtain a white-yellowish powder called g-C_3N_4.

2.3 Synthesis of g-C_3N_4/BiOBr

The composite was obtained through a co-precipitation method. Initially, 4.85 g of $Bi(NO_3)_3.5H_2O$ was dissolved in 200 mL of distilled water and stirred for 5 minutes to ensure a complete dissolution. Subsequently, 0.92 g of g-C_3N_4 powder was added to the solution, followed by continuous stirring for 10 min. Following this, 18 mL of acetic acid was added to the mixture, which was further stirred using a magnetic stirrer for 30 minutes. Afterward, 1.03 g of sodium bromide and 0.886 g of sodium acetate were simultaneously added as the bromide

precursor and buffering agent, respectively. The mixture was then stirred continuously for 2 hours to facilitate the formation of BiOBr in the presence of g-C_3N_4. The resulting suspension was aged for 12 hours, and the solid product was centrifuged. The precipitate was then washed several times using distilled water and ethanol until the pH of the wash solution reached approximately 5. The obtained precipitate was then dried on a hot plate at 65°C for 4 hours.

2.4 Synthesis of g-C_3N_4/BiOBr/pumice stone

To enhance the light accessibility, the composite obtained before was immobilized onto pumice stone through a surface modification and impregnation technique. Typically, pumice stones were washed and ultrasonicated thoroughly with distilled water several times to ensure the impurities were removed. The cleaned pumice stones were then dried under direct sunlight. A sol-gel suspension was prepared by mixing 1 gram of g-C_3N_4/BiOBr, 150 mL of distilled water, 150 mL of ethanol, and 1 mL of TEOS as a binding agent, then stirred for 30 minutes and sonicated for 10 minutes to ensure homogeneity. Afterward, 50 grams of the pre-cleaned pumice stones were added to the sol-gel mixture, followed by magnetic stirring for 20 minutes, and sonicating for 10 minutes to promote an even coating of the photocatalyst precursor on the pumice surface. The coated pumice stones were then filtered out and dried in an oven at 100°C for 1 hour to ensure firm adhesion and evaporation of residual solvents.

2.5 Characterizations of g-C_3N_4/BiOBr photocatalyst

The morphology and elemental composition of the synthesized photocatalyst were analyzed using a Scanning Electron Microscope (SEM, Thermo Scientific Quattro S, completed with EDS detector) at 10 kV and equipped with Energy Dispersive X-ray spectroscopy (EDX). The X-ray diffraction experiment was performed on an EMPYREAN diffractometer with Cu Kα radiation (λ = 0.15418 Å at 40 kV and 30 mA). The diffraction pattern was recorded from 5° to 90° with a step size of 0.02°. A Photoluminescence Microspectrometer Horiba Scientific iHR320 was used with a 325 nm laser beam to offer clues regarding the electron-hole recombination dynamics. Subsequently, X-ray photoelectron spectroscopy (XPS) was obtained using XPS Kratos AXIS SUPRA PLUS. The optical properties and bandgap values were determined using the Kubelka-Munk functions from UV-Visible Diffuse Reflectance Spectra (UV-Vis DRS, Agilent Cary 60 UV-Vis Spectrophotometer). The data were obtained in the range of 300-500 nm. The nanostructure was also ensured using the HRTEM FEI Tecnai G2 20 S-TWIN 200 kV to ensure the success of the composite synthesis catalyst and to measure the nanoscale material structure.

2.6 Development of the photocatalysis-electrocoagulation system

The photocatalysis-electrocoagulation reactor system used in this study was box-shaped (Figure 1) with internal dimensions of 10 x 10 x 8 cm, with quartz glass windows (10 x 10 cm) on the top side to illuminate effectively. The electrocoagulation section used an aluminum anode plate and a 316 stainless steel cathode with an area of 39 cm². The distance between the anode and cathode was set at 2 cm. A direct current of 2-5 V was applied throughout the process using a DC generator power supply (Zhaoxin RXN-605D, 60 V 5 A). In the same compartment, the photocatalysis process will occur on the surface of pumice containing g-C_3N_4/BiOBr nanocomposite floating on the surface of seawater during the observation. The

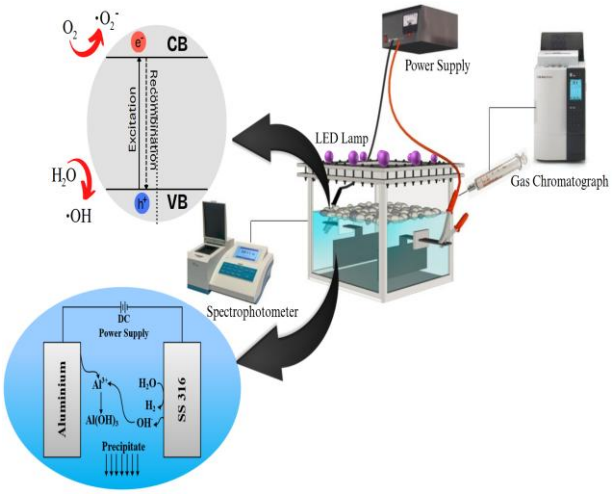

Fig 1. Photocatalysis-Electrocoagulation System

pumice used was 1-1.5 cm in size, with a volume ranging from 0.52-1.77 cm³. A total of 37 grams of pumice was used in each experiment. The light source consisted of 9 EPILEDS 3 W LED lamps (λp= 410–420 nm), which were positioned on the top side of the reactor. The reactor was made airtight to facilitate hydrogen production monitoring and equipped with copper wires and a DC power supply to deliver voltage to the anode and cathode. Before the process begins, purging is carried out to clean the solution used from dissolved oxygen content, so that the possibility of superoxide radical formation can be minimized. The reactor was mechanically stirred to ensure homogeneous mixing, while electrocoagulation was performed under the applied electrical potential.

2.7 Assessment of the photocatalysis-electrocoagulation performance

The photocatalysis and electrocoagulation were conducted in the system reactor filled with 500 mL of electrolyte (initial concentration of 10% seawater and 10 mg/L methylene blue) and 37 grams of the g-C_3N_4/BiOBr/pumice stone. The seawater used has been analyzed and shows the presence of Ca (3900 ppm), Mg (1300 ppm), and Na (3700 ppm). The sampling of the liquid solution was collected at certain time intervals during the experiment period. The methylene blue absorbance was measured using the Spectrophotometer Genesys 10S UV-Vis at 666 nm. Absorbance and concentration reduction were calculated using Equation (1).

$$\%\ \boldsymbol{MB\ Decolorization} = \frac{C_0 - C}{C_0} \times 100 \qquad (1)$$

In this context, C_0 and C denote the concentrations of methylene blue in mg/L (ppm) at the initial and specific time intervals, respectively. The hydrogen production was determined using gas chromatography (Shimadzu GC-2014) equipped with a molecular sieve (MS) hydrogen 5A column, using argon as the carrier gas with a known retention time. Sampling was performed at least in duplicate, and the average values were used.

3. Results and Discussion

3.1 Characterization of X-ray diffraction (XRD) analysis

The crystal structures formed during calcination based on crystal size were analyzed using X-ray diffraction (XRD), as

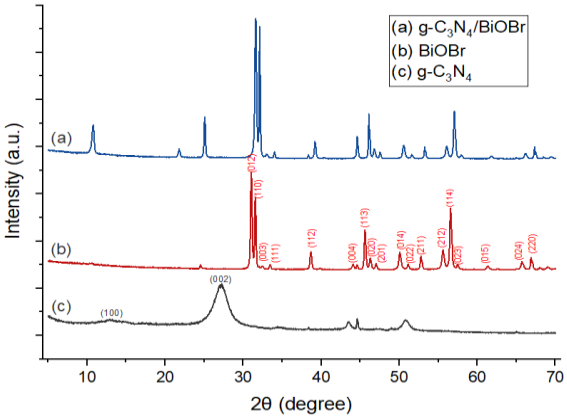

Fig 2. XRD pattern of (a) g-C_3N_4/BiOBr, (b) BiOBr, and (c) g-C_3N_4

shown in Figure 2. The diffraction peaks were observed corresponding to the structural components of the photocatalyst. The g-C_3N_4 peaks appeared at 2θ = 13.1°, 27.2°, 43.5°, 44.7°, and 50.9°, indicating that the crystal type was tri-s-triazine, while BiOBr appeared at 2θ = 10.8°, 24.6°, 31°, 31.5°, 32.5°, 33.4°, 38.8°, 44°, 44.7°, 45.8°, 46.2°, 47°, 50.2°, 31.1°, 52.8°, 55.7°, 56.5°, and 58.4°, indicating that the crystal type was tetragonal (C. Li *et al.,* 2020). The crystallite size of the tri-s-triazine was 6.43 nm, and the tetragonal was 34.41 nm. These results are confirmed by the JCPDS data for g-C_3N_4 (No. 87-1526) and BiOBr (No. 09-0393) (Alizadeh *et al.*, 2019; Riyadh Atta *et al.*, 2023). The difference in crystallite size between g-C_3N_4 (6.43 nm) and BiOBr (34.41 nm) could potentially influence the formation of a heterojunction interface. Smaller g-C_3N_4 crystallites could provide more flexible contact with the larger BiOBr domains, thereby increasing physical interfacial contact and facilitating charge migration across the heterojunction. Smaller crystallite sizes are generally associated with higher surface area-to-volume ratios, which may contribute to increased availability of active sites for photocatalytic reactions. The interpretation of these XRD analysis results is primarily limited to providing qualitative structural information, rather than direct evidence of interfacial charge transfer.

3.2. Morphological analysis using SEM-EDX

Figures 3(a), (b), and (c) depict the morphology of g-C_3N_4, BiOBr, and g-C_3N_4/BiOBr (1:0.67) based on SEM analysis. It can be seen that g-C_3N_4 synthesized through two-stage calcination had irregular lamellar aggregates. The open mesoporous structure of g-C_3N_4 and two-dimensional layered morphology improved its photocatalytic performance by facilitating light

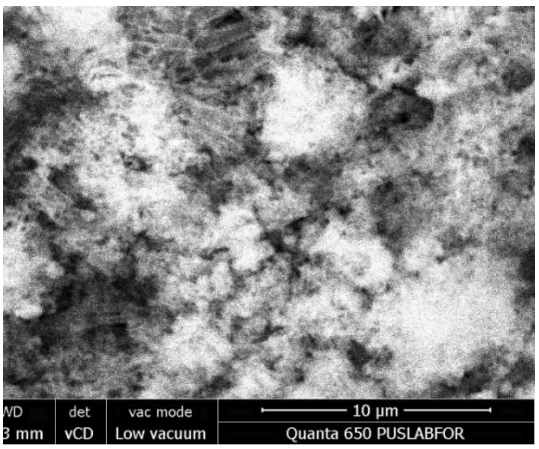

(a)

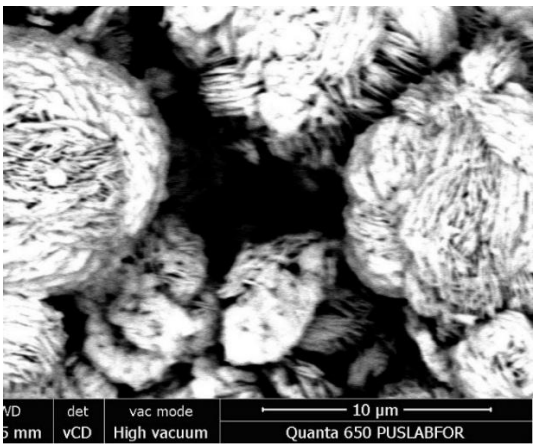

(b)

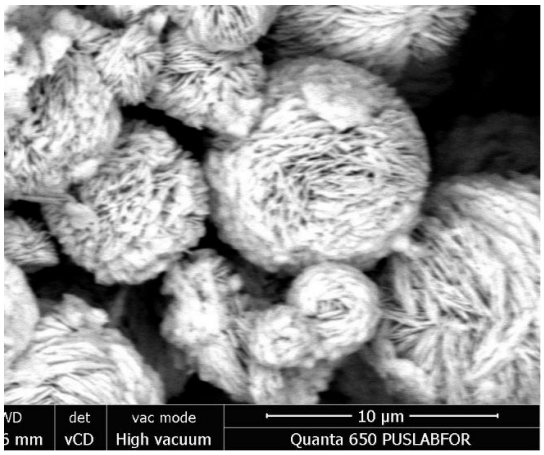

(c)

Fig 3. SEM Image of (a) g-C_3N_4; (b) BiOBr; and (c) g-C_3N_4/BiOBr (1:0.67)

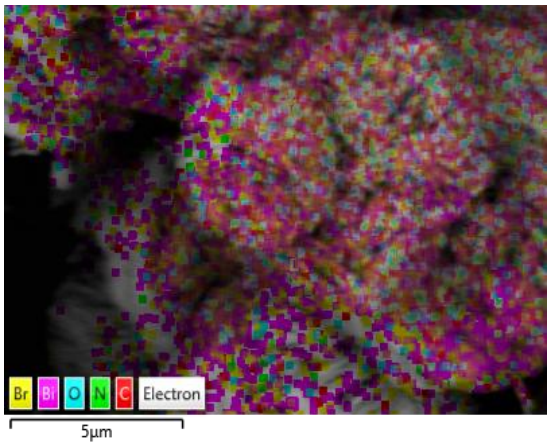

Fig 4. EDX elemental mapping of g-C_3N_4/BiOBr (1:0.67)

absorption and effective photoinduced charge migration along the 2D plane. In addition to BiOBr, in the results of research conducted by Yang, L., *et al.* (2019), through the same synthesis method, a similar morphology (flower-like) was obtained (Yang *et al.*, 2019). Meanwhile, the g-C_3N_4/BiOBr (1:0.67) nanocomposite was the same morphological combination of both photocatalysts. However, the presence of g-C_3N_4 was less visible because it was covered by BiOBr, considering the difference in crystal particle size.

As shown on Figure 4, the EDX analysis of g-C_3N_4/BiOBr (1:0.67) confirmed that the g-C_3N_4 was successfully composited in BiOBr. In the g-C_3N_4/BiOBr (1:0.67) composite, the presence of BiOBr was more dominant due to the much higher crystal size when identified through XRD, so the mass percentages of the C and N components in the g-C_3N_4/BiOBr (1:0.67) composite were few and in EDX were only measured through one location. In addition, in the SEM of g-C_3N_4/BiOBr (1:0.67), it can be seen that BiOBr was not very hollow, implying that g-C_3N_4 with smaller crystals filled the voids in BiOBr.

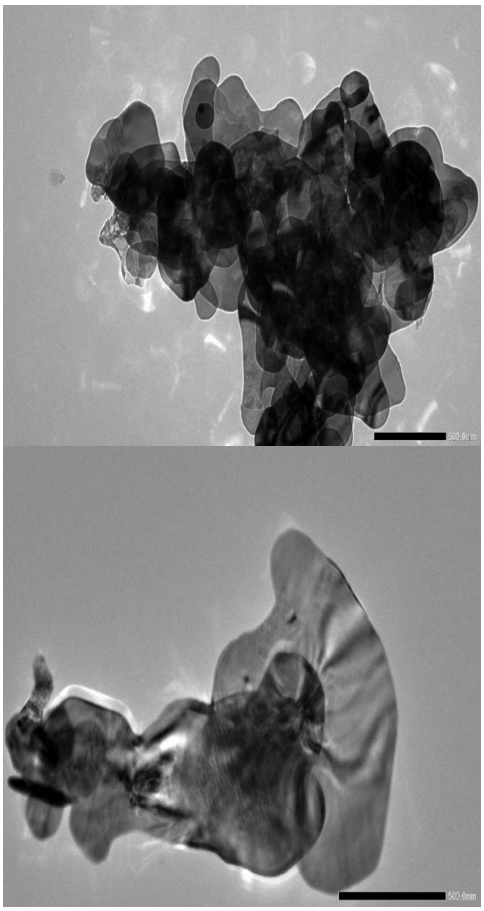

Fig 5. TEM image for g-C_3N_4/BiOBr: (a) Aggregated nanoparticles of g-C_3N_4/BiOBr, and (b) Nanosheet morphology of g-C_3N_4/BiOBr

3.3. Transmission Electron Microscope (TEM)

Transmission electron microscopy (TEM) characterization was performed to obtain a clearer picture of the distribution and contact proximity between g-C_3N_4 and BiOBr as a nanocomposite. Figure 5(a) illustrates loose agglomeration between particles with varying degrees of transparency. This difference indicates non-uniform sheet thickness, with darker areas indicating thicker ones. Figure 5(b) provides a clearer picture of the thin, sheet-like surface that curves. This structure supports the presence of folded or curled 2D layers, typical of modified g-C_3N_4-based materials. TEM results complement the SEM observations by providing a clearer visualization of the nanosheet morphology and physical proximity between the g-C_3N_4 and BiOBr domains within the composite. These images confirm the layered structural features of the material; however, the absence of clearly visible lattice lines suggests that TEM primarily supports morphological characterization rather than direct evidence of interfacial heterojunction formation or electronic interactions.

3.4. Photoluminescence spectroscopy

Figure 6 shows the photoluminescence characterization results of the g-C_3N_4, BiOBr, and g-C_3N_4/BiOBr photocatalysts. The results indicated that nanocomposite formation successfully suppressed the recombination rate of holes and electrons. Compared with g-C_3N_4, the photoluminescence peak of the g-C_3N_4/BiOBr nanocomposite was lower, suggesting

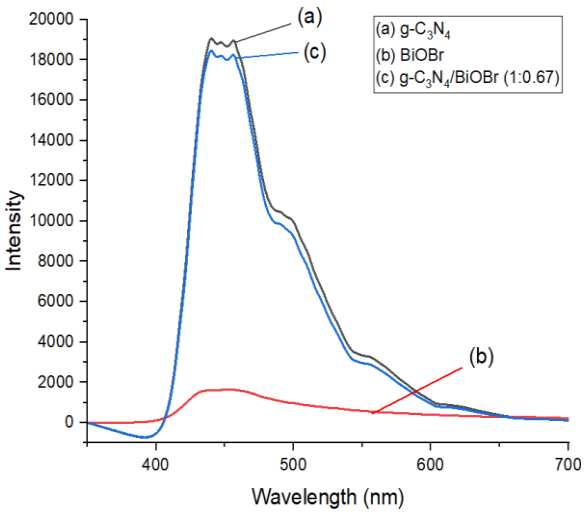

Fig 6. Photoluminescence spectra of (a) g-C_3N_4, (b) BiOBr, and (c) g-C_3N_4/BiOBr (1:0.67)

weaker electron transfer. This lower peak showed reduced electron-hole recombination, which was desirable for improved photocatalytic performance. The decrease in PL intensity in the composite compared to pure g-C_3N_4 is a strong indication of effective interfacial interactions, where electrons from the CB of g-C_3N_4 could move to the CB of BiOBr, while holes move from the VB of BiOBr to the VB of g-C_3N_4.

The interpretation of the reduced PL intensity results for the g-C_3N_4 composite compared to pure g-C_3N_4 is qualitative. This is because we did not use charge carrier lifetime measurements, and therefore, we do not obtain information regarding the quantitative aspects of the PL characterization.

3.5. UV-Vis DRS

The UV-Vis DRS analysis compared the optical properties of g-C_3N_4, BiOBr, g-C_3N_4/BiOBr (1:0.5), g-C_3N_4/BiOBr (1:0.67), g-C_3N_4/BiOBr (1:1), g-C_3N_4/BiOBr (1:1.5), and g-C_3N_4/BiOBr (1:2) composites by evaluating their absorbance spectra and bandgap energies. The absorbance spectra in Figure 7A exhibit that all the various g-C_3N_4/BiOBr had stronger light absorption in the visible region (460-469 nm), which is also confirmed by other research (Wu *et al.,* 2019; X. Zhang *et al.,* 2024). This indicates that the photocatalyst material's compositing causes the nanocomposite's bandgap energy to increase the absorbance and wavelength more than that of the pure material.

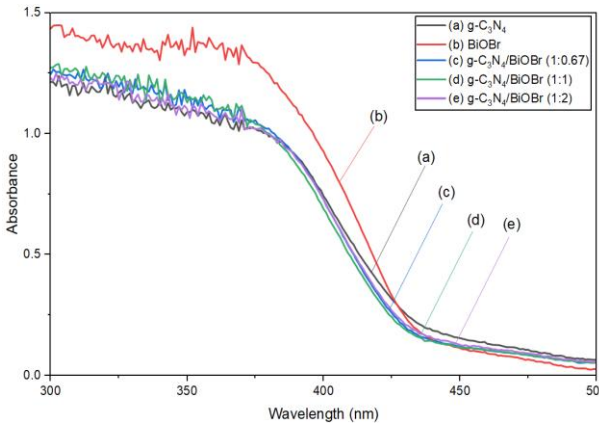

Fig 7A. UV-Vis DRS spectrum of (a) g-C_3N_4, (b) BiOBr, (c) g-C_3N_4/BiOBr (1:0.67), (d) g-C_3N_4/BiOBr (1:1), and (e) g-C_3N_4/BiOBr (1:2)

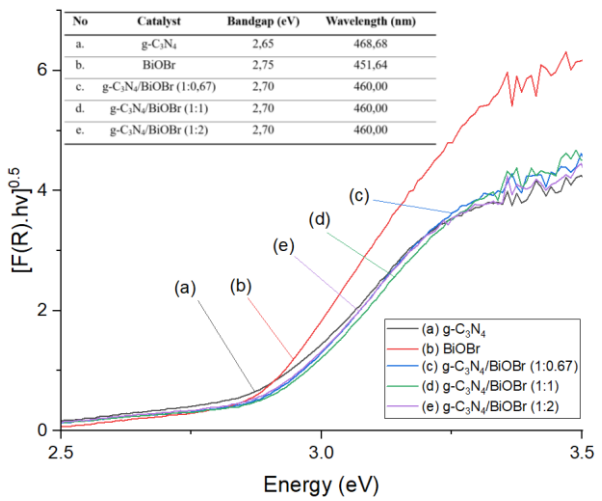

Fig 7B. Tauc plot of (a) g-C_3N_4, (b) BiOBr, (c) g-C_3N_4/BiOBr (1:0.67), (d) g-C_3N_4/BiOBr (1:1), and (e) g-C_3N_4/BiOBr (1:2)

Figure 7B shows the Tauc plot derived from the Kubelka-Munk function. The results displayed a slight narrowing of the bandgap energy (Eg) for g-C_3N_4 and BiOBr compared to g-C_3N_4/BiOBr. The measurement of the g-C_3N_4 bandgap was at 2.65 eV, consistent with typical g-C_3N_4 values (Zuluaga *et al.,* 2015), and the BiOBr bandgap was at 2.75 eV, consistent with typical BiOBr values (Saddique *et al.,* 2023). Meanwhile, the g-C_3N_4/BiOBr composite exhibited a lower bandgap of 2.7 eV due to BiOBr, a semiconductor with 2.75 eV (Song *et al.,* 2023; B. Zhang *et al.,* 2021).

The obtained intermediate value is analyzed as the apparent optical bandgap energy, which represents the combined absorption contribution of both semiconductors. This value is not a direct indication of heterojunction formation, which can alter the bandgap. In this context, the effect of heterojunction formation is more visible as an increase in charge separation efficiency or a successful reduction in recombination, resulting in improved photocatalytic performance. Meanwhile, the DRS results primarily indicate an effect of increasing the composite's absorbance upon light exposure.

3.6. X-ray photoelectron spectroscopy (XPS)

Oxidation state analysis of the component present on the surface of the g-C_3N_4/BiOBr nanocomposite is necessary to ensure its suitability with the desired nanocomposite characteristics. The X-ray Photoelectron Spectroscopy (XPS) characterization was used to identify the surface of the g-C_3N_4/BiOBr nanocomposite. The broad survey spectrum (Figure 8(a)) shows the presence of peaks corresponding to the binding energies of C, N, O, Br, and Bi, confirming the primary chemical composition of the nanocomposite.

The sp2 carbon bond in the N-C=N fragment of the g-C_3N_4 heptazine framework was linked to a prominent peak in the high-resolution C1s spectra (Figure 8(b)) with a binding energy of roughly 288.2 eV. This peak's existence suggests that following composite creation, the fundamental structure of g-C_3N_4 was preserved.

There were two peaks in the N1 spectra (Figure 8(c)) at roughly 398.6 eV and 400.1 eV. The sp^2 nitrogen in the heptazine ring's C-N=C bond was linked to the first peak, whereas the terminal amino group or the three-coordinated nitrogen (N-$(C)_3$) was linked to the second peak. The existence of an unbroken g-C_3N_4 polymer framework is supported by this distribution.

The major peak in the O 1s spectrum (Figure 8(d)) was located at 529.9 eV and was caused by oxygen in the $[Bi_2O_2]^{2+}$ layer of BiOBr. The layered structure was partly formed by this oxygen, an essential component of the BiOBr crystal lattice.

The Br^- state in the BiOBr lattice is represented by a peak in the Br $3d_{5}/_{2}$ spectrum (Figure 8(e)) for bromine, which was located at 67.8 eV. Two peaks at about 182.4 eV and 185.0 eV in the Br $3p_{3}/_{2}$ spectrum (Figure 8(g)) were also linked to bromide species in the crystal structure.

The Bi 4f spectrum (Figure 8(f)) displayed two distinctive peaks at 159.1 eV (Bi $4f_{7}/_{2}$) and 164.4 eV (Bi $4f_{5}/_{2}$) that are compatible with the Bi^{3+} oxidation state in BiOBr. Bi $4d_{5}/_{2}$ (Figure 8(i)) was found at around 441.9 eV and 466.4 eV, whereas the Bi $5d_{5}/_{2}$ spectrum (Figure 8(h)) showed two peaks at about 24.7 eV and 27.0 eV. These numbers indicate that the BiOBr phase was well-formed in the composite and align with data from the literature for pure BiOBr.

Overall, the XPS results indicate that the resultant nanocomposite contains BiOBr with a $Bi^{3+}/Br^{-}/O^{2-}$ composition consistent with its regular structure, and g-C_3N_4 with an intact heptazine framework. The absence of obvious binding energy shifts observed in the resulting XPS spectra indicates that the surface states of g-C_3N_4 and BiOBr remain largely unchanged after composite formation. This implies that the interaction between g-C_3N_4 and BiOBr is relatively weak and dominated by physical interfacial contact rather than chemical bonding. This fact represents a limitation of the resulting composite, although the photocatalytic performance still demonstrates improved capabilities in degrading organic pollutants and producing hydrogen.

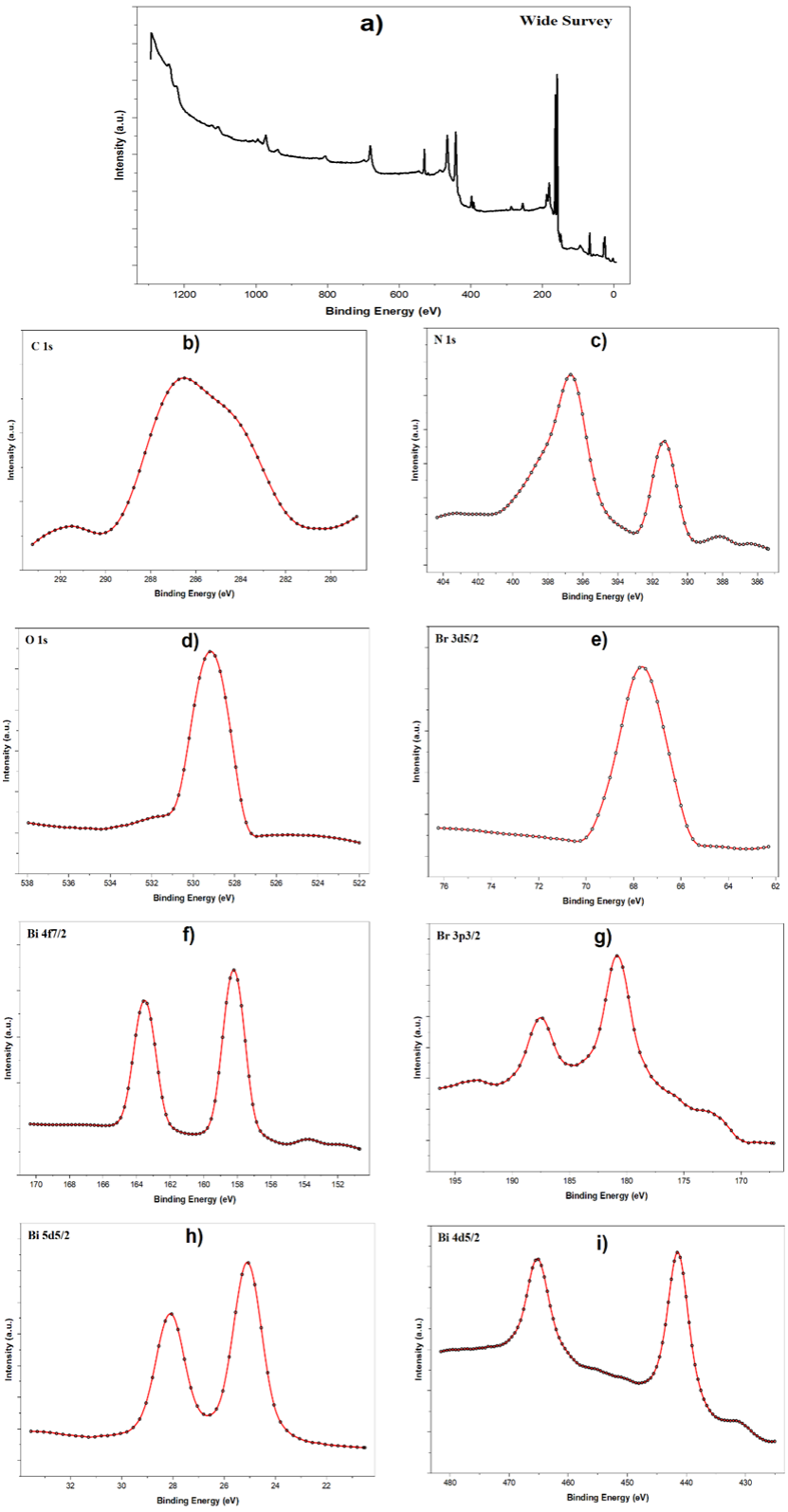

Fig 8. The XPS spectra for a) Wide Survey, b) C 1s, c) N 1s, d) O 1s, e) Br 3d5/2, f) Bi 4f7/2, g) Br 3p3/2, h) Bi 5d5/2, and (i) Bi 4d5/2

3.7 Analysis of photocatalytic and electrocoagulation performances

The performance of photocatalysis and electrocoagulation processes, individually and simultaneously, was tested to determine the optimal process capability in terms of photocatalyst materials with various composites, seawater concentration, and voltages in degrading pollutants while producing hydrogen. In this study, photocatalyst performance was assessed through the decolorization of methylene blue (MB), which indicates photocatalytic activity for pollutant degradation. The decrease in MB concentration was monitored using a spectrophotometer as an initial approach to assess the potential of photocatalysts in the pollutant oxidation process. The hydrogen gas produced was monitored by taking gas samples from the process system and analyzing them using a gas chromatograph.

3.8. MB decolorization analysis

Through the % decolorization data obtained when running for 3 hours, as shown in Figure 9, it can be seen that the highest percent decolorization of MB was obtained by the composited catalyst, which verifies that the composite between g-C_3N_4 and BiOBr decreases the recombinant rate, which is indicated by the decrease in emission intensity in the photoluminescence (PL) characterization results. This decrease in intensity suggests that fewer electron-hole pairs (e^-/h^+) underwent radiative recombination, so more electrons and holes participated in the photocatalytic reaction. This occurred due to the formation of a type II heterojunction, or Z-scheme, between g-C_3N_4 and BiOBr, facilitating more efficient charge separation and the transfer of electrons and holes to more favorable energy positions. Thus, the g-C_3N_4/BiOBr composite could significantly increase the photocatalytic activity compared to the single material, resulting in higher decolorization of methylene blue.

3.9. The seawater effect on photocatalytic

The g-C_3N_4/BiOBr catalyst (1:0.67) was then tested to determine the effect of seawater on the decolorization of methylene blue. Based on the tests obtained, as presented in Figure 10, it can be seen that the higher the seawater

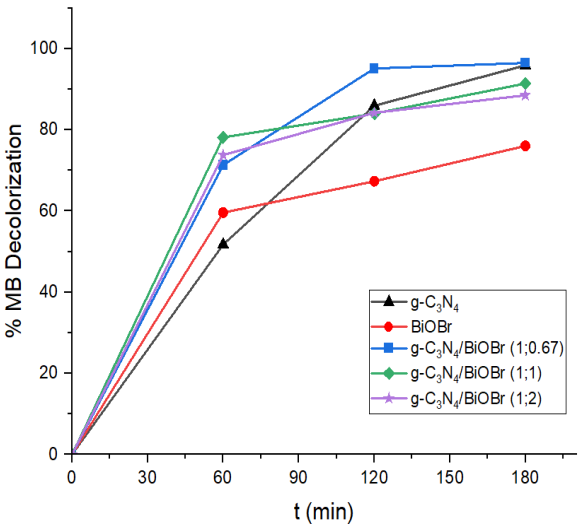

Fig 9. MB decolorization efficiency of g-C_3N_4, BiOBr, g-C_3N_4/BiOBr (1:0.5), g-C_3N_4/BiOBr (1:0.67), g-C_3N_4/BiOBr (1:1), g-C_3N_4/BiOBr (1:1.5), and g-C_3N_4/BiOBr (1:2)

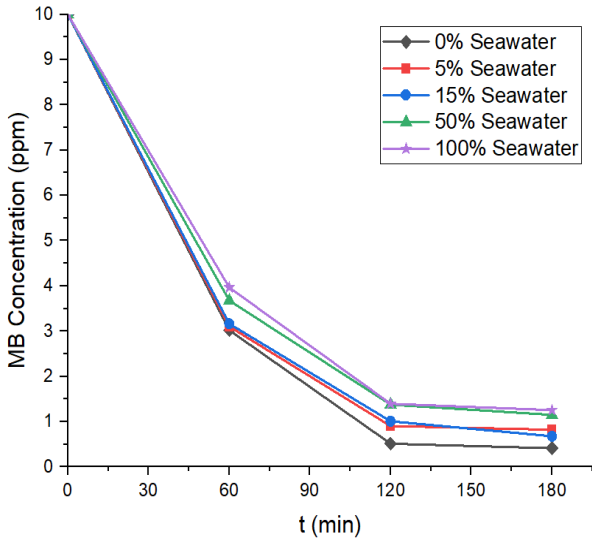

Fig 10. Effect of seawater concentration on photocatalysis in MB decolorization

concentration in the methylene blue solution, the more the decolorization ability of the photocatalyst material would decrease. This was due to salt ions in seawater competing with or neutralizing hydroxyl radicals formed through oxidation reactions (Gutowski & Kowalczyk, 2013; Yuan *et al.*, 2022). As a result, hydroxyl radicals interacting with these ions became less reactive, so the effectiveness in photo-decolorization decreased.

3.10. Analysis of electrocoagulation performance

The performance of the electrocoagulation process was tested to determine the ability of the combination of aluminum and stainless steel 316 electrodes to coagulate methylene blue contained in seawater and the amount of hydrogen that could be produced.

Figure 11(a) illustrates the experimental results of voltage variations in electrocoagulation, indicating that the greater the voltage applied, the greater the volume of hydrogen formed and the mass of coagulant. This is because a higher voltage will encourage the electrocoagulation reaction rate to be faster, as in the voltaic series theory. However, the varied voltage was limited to a maximum of 5V to avoid the possibility of chlorine gas (Cl_2) formation, given the large number of Cl^- ions in seawater, and not too close to the standard potential of other reactions, because, of course, there are circuit barriers so that overpotential is needed. The data denotes that at a voltage of 2V, no gas was formed for 30 minutes due to the tiny current not being enough to trigger the electrocoagulation reaction optimally. In addition, the increase in gas production at 4V and 5V was not very significant, so with the efficiency and effectiveness of the reaction, the 4V voltage is a suitable choice to be used as a reference in the next process.

After obtaining the optimal voltage to produce hydrogen and coagulate methylene blue, it was used to determine the optimal seawater concentration before the electrocoagulation process was combined with the photocatalysis process. The duration of this test was limited to 2 hours each with a voltage of 4 volts due to the slow production of hydrogen at small seawater concentrations.

Observation results revealed that increasing the seawater concentration in the methylene blue solution significantly increased the efficiency of the electrocoagulation process up to a certain point, as shown in Figure 11(b). At 0% seawater

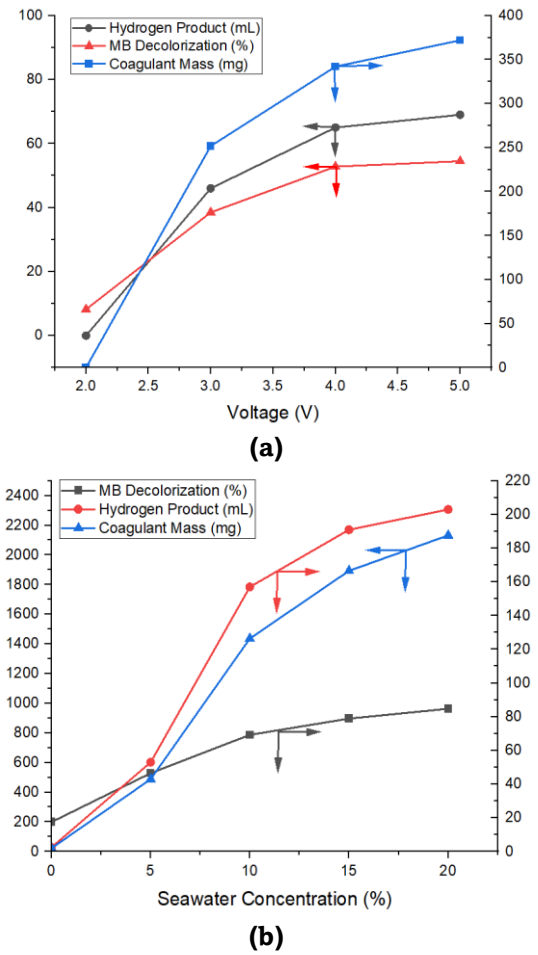

Fig 11. The performance of the electrocoagulation process in its ability to remove MB and produce hydrogen based on the following observed variables: (a) effect of voltage (10% seawater, 2-hour process); (b) effect of seawater concentration (voltage = 2V, 2-hour process)

concentration, MB decolorization was very low, only 17.51%, with minimal hydrogen formation and coagulant mass (2.5 mL and 21.7 mg, respectively). However, when the seawater concentration was increased to 15%, the decolorization efficiency increased dramatically to 78.87%, characterized by a decrease in MB concentration from 10 ppm to 2.15 ppm, as well as a significant increase in hydrogen volume (191 mL) and coagulant mass (1893 mg). This indicates that ions in seawater, such as Na^+, Ca^{2+}, and Mg^{2+}, play an important role in accelerating coagulant formation and supporting the destabilization process of MB particles through adsorption and precipitation mechanisms.

Nevertheless, although the 20% seawater concentration resulted in slightly higher hydrogen product and coagulant mass (203 mL and 2132 mg), its MB decolorization efficiency was only slightly better than the 15% concentration. This increase is practically insignificant, while energy consumption and the number of ions involved will be greater at 20% concentration.

A linear increase in seawater concentration with increasing coagulant quantity does not necessarily increase pollutant removal efficiency proportionally. This may be due to the reduced stability of the $Al(OH)_3$ floc due to the high ionic strength, which results in compression of the electrical double layer and reduced aggregate formation efficiency. High-salinity solution systems containing Mg^{2+} and Ca^{2+} also have the potential for competitive reactions to form $Mg(OH)_2$ and $CaCO_3$, reducing hydroxide consumption for $Al(OH)_3$ floc formation and impacting the performance of the electrocoagulation process in pollutant removal.

Therefore, a 15% concentration was chosen as the optimum condition, giving almost comparable results to 20% but with better material and energy efficiency. This confirms an optimum point in utilizing seawater salinity to efficiently support the electrocoagulation process without overloading the reaction system.

3.11. Analysis of photocatalytic-electrocoagulation performance

Both photocatalysis and electrocoagulation were then combined into a single reactor once the ideal catalyst composition, applied voltage, and saltwater concentration had been e stablished for each process separately. This integration aimed to assess how effectively the two processes integrate to produce hydrogen from seawater and degrade organic pollutant simultaneously. Observations were conducted for 2 hours with a voltage of 4 volts and at a seawater concentration of 15%.

It can be seen from Figures 12(a) and (b) that the data indicate that pH variation significantly affected the performance of the combined photocatalysis-electrocoagulation process, especially in terms of gas production and efficiency of methylene blue concentration reduction. At low (acidic) pH, such as pH 1 and 3, the hydrogen produced was higher (228 mL and 211 mL, respectively, with a composite weight of 37 g), compared to pH 7, which only produced 138 mL. This increase

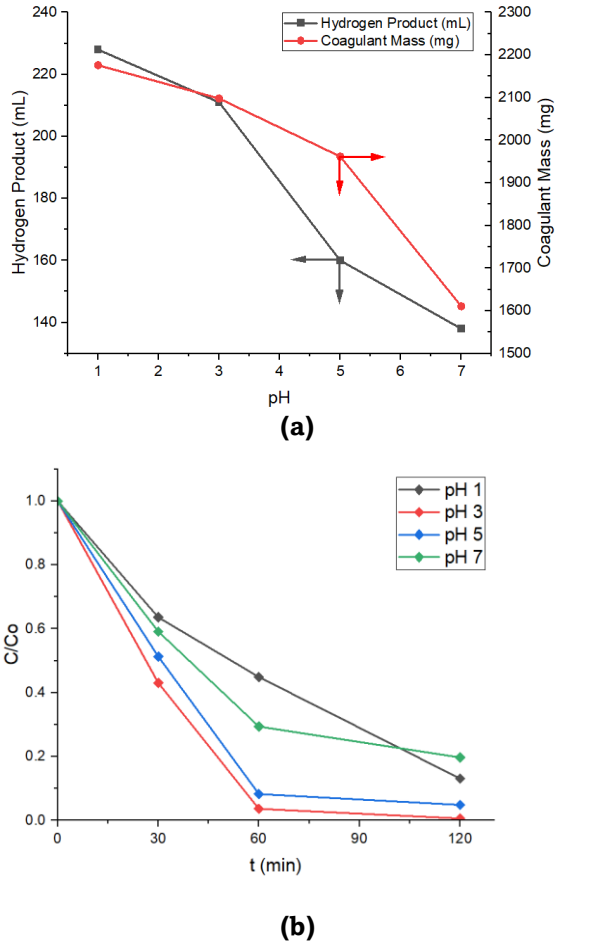

Fig 12. Effect of pH on photocatalytic-electrocoagulation in: (a) hydrogen production and coagulant formation; (b) MB decolorization (with 15% seawater concentration, voltage 4V)

is attributed to the high concentration of H^+ ions in an acidic atmosphere, which increases the conductivity of the solution so that the electric current becomes more efficient in producing the electrocoagulation reaction (Nwabanne *et al.,* 2017). This favors the formation of more gas bubbles and accelerates coagulant formation. The effectiveness of MB decolorization also appeared higher at pH 3, where the % decolorization of MB reached 99.37%.

On the other hand, at pH 1, the coagulant formed was too much, causing a shading effect on the photocatalysis process. This condition inhibited the optimal absorption of photons by the photocatalyst surface, so the performance of photocatalysis decreased, and the more dominant process was electrocoagulation. Using the best combination of conditions (optimal catalyst, 4V voltage, and 15% seawater), pH variation is the key to fine-tuning the process performance. These results denote that pH 3 is the optimum point, where MB decolorization efficiency is very high and hydrogen production remains large without extreme acid overload, as at pH 1. As the pH decreases, the current increases, indicating more electron flow and increased conductivity. If the pH continues to decrease and the current continues to increase, it is a sign that more electrons are being produced, producing more hydrogen and coagulant. In this study, it is limited to only varying the pH with 15% seawater concentration. To achieve more optimal results, it is necessary to vary several parameters, which will still be discussed in the next study.

4. Conclusion

This study developed an integrated photocatalysis–electrocoagulation (P-E) system that successfully enabled simultaneous hydrogen production and pollutant degradation from seawater, specifically methylene blue. Utilizing a g-C_3N_4/BiOBr composite with a 1:0.67 mole ratio, the system achieved high photocatalytic performance, degrading 96.49% of methylene blue within 180 minutes. This also indicates that pumice stones effectively absorb light to activate the photocatalyst. Under optimal conditions (4 V, 15% seawater concentration, pH 3), the combined process exhibited strong synergistic effects, reaching 99.37% pollutant removal and hydrogen production of 211 mL. These findings confirm that coupling visible-light-driven catalysis with electrochemical coagulation offers an efficient and sustainable approach to seawater-based hydrogen generation and water purification.

Acknowledgments

The authors would like to acknowledge the funding provided by the Directorate General of Research and Development, Ministry of Higher Education, Science, and Technology (No: PKS-505/UN2.RST/HKP.05.00/2025). The statements made herein are solely the responsibility of the authors

Author Contributions: M.F.B.: Principal researcher responsible for data collection and initial data interpretation. S: Provided the initial concept and research ideas, directed the research methodology, and reviewed and revised the manuscript. All authors have read and agreed to the published version of the manuscript.

Conflicts of Interest: The authors declare that there are no conflicts of interest regarding the publication of this paper. All funding and support received have not influenced the design, execution, or conclusions.

References

Al-Ajmi, F., Al-Marri, M., & Almomani, F. (2025). Electrocoagulation Process as an Efficient Method for the Treatment of Produced Water Treatment for Possible Recycling and Reuse. *Water (Switzerland), 17*(1). https://doi.org/10.3390/w17010023

Ali, S., Badar, M. S., Daniyal, Nikkhah, A., Fen, C. S., Nouri, A., Mohammad, A. W., Lun, A. W., Nourigheimasi, F., Ng, L. Y., & Mahmoudi, E. (2024). Progress in nanomaterial-driven redox reactions for water purification: A critical review. In *Desalination and Water Treatment* (Vol. 320). Elsevier B.V. https://doi.org/10.1016/j.dwt.2024.100616

Alizadeh, T., Nayeri, S., & Hamidi, N. (2019). Graphitic carbon nitride (g-C3N4)/graphite nanocomposite as an extraordinarily sensitive sensor for sub-micromolar detection of oxalic acid in biological samples. *RSC Advances*, *9*(23), 13096–13103. https://doi.org/10.1039/c9ra00982e

Arenas, J. P., Parra, C. C., Rebolledo, J., & Venegas, R. (2025). Granular Pumice Stone: A Natural Double-Porosity Sound-Absorbing Material. *Buildings*, *15*(4). https://doi.org/10.3390/buildings15040557

Badruzzaman, A., Karagoz, S., & Eljack, F. (2025). Sustainable-green hydrogen production through integrating electrolysis, water treatment and solar energy. *Frontiers in Chemical Engineering*, *7*. https://doi.org/10.3389/fceng.2025.1526331

Boinpally, S., Kolla, A., Kainthola, J., Kodali, R., & Vemuri, J. (2023). A state-of-the-art review of the electrocoagulation technology for wastewater treatment. In *Water Cycle* (Vol. 4, pp. 26–36). KeAi Communications Co. https://doi.org/10.1016/j.watcyc.2023.01.001

Bonifaz García, H. (n.d.). *Physical properties of pumice and its behavior as a coarse aggregate in concrete*. https://www.researchgate.net/publication/329526815

Cheekatamarla, P. (2024). Hydrogen and the Global Energy Transition—Path to Sustainability and Adoption across All Economic Sectors. *Energies*, *17*(4). https://doi.org/10.3390/en17040807

Gupta, A., Likozar, B., Jaidka, S. (2025). A review on photocatalytic seawater splitting with efficient and selective catalysts for hydrogen evolution reaction. Renewable and Sustainable Energy Reviews, Vol 208, 115074. https://doi.org/10.1016/j.rser.2024.115074

Gutowski, M., & Kowalczyk, S. (2013). *A study of free radical chemistry: their role and pathophysiological significance*. www.actabp.pl

Harish, S., Archana, J., Sabarinathan, M., Navaneethan, M., Nisha, K. D., Ponnusamy, S., Muthamizhchelvan, C., Ikeda, H., Aswal, D. K., & Hayakawa, Y. (2017). Controlled structural and compositional characteristic of visible light active ZnO/CuO photocatalyst for the degradation of organic pollutant. *Applied Surface Science*, *418*, 103–112. https://doi.org/10.1016/j.apsusc.2016.12.082

Hayat, A., Al-Sehemi, A. G., El-Nasser, K. S., Taha, T. A., Al-Ghamdi, A. A., Jawad Ali Shah Syed, Amin, M. A., Ali, T., Bashir, T., Palamanit, A., Khan, J., & Nawawi, W. I. (2022). Graphitic carbon nitride (g–C3N4)–based semiconductor as a beneficial candidate in photocatalysis diversity. In *International Journal of Hydrogen Energy* (Vol. 47, Issue 8, pp. 5142–5191). Elsevier Ltd. https://doi.org/10.1016/j.ijhydene.2021.11.133

Hosseini, S. F., Seyed Dorraji, M. S., & Rasoulifard, M. H. (2023). Boosting photo-charge transfer in 3D/2D TiO2@Ti3C2 MXene/Bi2S3 Schottky/Z-scheme heterojunction for photocatalytic antibiotic degradation and H2 evolution. *Composites Part B: Engineering*, *262*. https://doi.org/10.1016/j.compositesb.2023.110820

Imam, S. S., Adnan, R., & Mohd Kaus, N. H. (2021). The photocatalytic potential of BiOBr for wastewater treatment: A mini-review. In *Journal of Environmental Chemical Engineering* (Vol. 9, Issue 4). Elsevier Ltd. https://doi.org/10.1016/j.jece.2021.105404

Imran, S., & Hussain, M. (2024). Emerging trends in water splitting innovations for solar hydrogen production: Analysis, comparison, and economical insights. *International Journal of Hydrogen Energy*, *77*, 975–996. https://doi.org/10.1016/j.ijhydene.2024.06.254

Jia, J., Seitz, L. C., Benck, J. D., Huo, Y., Chen, Y., Ng, J. W. D., Bilir, T., Harris, J. S., & Jaramillo, T. F. (2016). Solar water splitting by photovoltaic-electrolysis with a solar-to-hydrogen efficiency over

30%. *Nature Communications*, *7*. https://doi.org/10.1038/ncomms13237

Khan, M.A., Al-Attas, T., Roy, S., Rahman, M.M., Ghaffour, N., Thangadurai, V., Larter, S., Hu, J., Ajayan, P.M., Kibria, M.G. (2021). Seawater electrolysis for hydrogen production: a solution looking for a problem? *Energy and Environment Science*, 14, 4831-4839. https://doi.org/10.1039/D1EE00870F

Li, C., Wang, B., Zhang, F., Song, N., Liu, G., Wang, C., & Zhong, S. (2020). Performance of Ag/BiOBr/GO composite photocatalyst for visible-light-driven dye pollutants degradation. *Journal of Materials Research and Technology*, *9*(1), 610–621. https://doi.org/10.1016/j.jmrt.2019.11.001

Li, R., & Li, C. (2017). Photocatalytic Water Splitting on Semiconductor-Based Photocatalysts. In *Advances in Catalysis* (Vol. 60, pp. 1–57). Academic Press Inc. https://doi.org/10.1016/bs.acat.2017.09.001

Madankar, R., Umekar, M., Bhusari, G., Mondal, A., Raish, M., Afzal, M., Norek, M., & Chaudhary, R. (2025). Rapid synthesis of graphitic carbon nitride nanosheets as an efficient adsorbent for removal of Methylene Blue and Rhodamine B from Aqueous Solutions. *Scientific Reports*, *15*(1), 28999. https://doi.org/10.1038/s41598-025-13645-5

Mechelhoff, M., Kelsall, G. H., & Graham, N. J. D. (2013). Electrochemical behaviour of aluminium in electrocoagulation processes. *Chemical Engineering Science*, *95*, 301–312. https://doi.org/10.1016/j.ces.2013.03.010

Meng, L., Qu, Y., & Jing, L. (2021). Recent advances in BiOBr-based photocatalysts for environmental remediation. *Chinese Chemical Letters*, *32*(11), 3265–3276. https://doi.org/10.1016/j.cclet.2021.03.083

Muttaqin, R., Pratiwi, R., Ratnawati, Dewi, E. L., Ibadurrohman, M., & Slamet. (2022). Degradation of methylene blue-ciprofloxacin and hydrogen production simultaneously using combination of electrocoagulation and photocatalytic process with Fe-TiNTAs. *International Journal of Hydrogen Energy*, *47*(42), 18272–18284. https://doi.org/10.1016/j.ijhydene.2022.04.031

Nazaruddin, D. A., Muchtar, A., Bahar, A., Muqtada, M., & Khan, A. (2014). *Preliminary Study on Potentials of Pumice as the New Material for Floating Devices and Buoy Products*. https://doi.org/10.5176/2335-6774_1.2.13

Nwabanne, J. T., Chiedozie, C., Nwabanne, J. T., & Obi, C. C. (2017). *Abattoir Wastewater Treatment by Electrocoagulation Using Iron Electrodes*. www.pelagiaresearchlibrary.com

Pelawi, L. F., Slamet, S., & Elysabeth, T. (2020). Combination of electrocoagulation and photocatalysis for hydrogen production and decolorization of tartrazine dyes using CuO-TiO2 nanotubes photocatalysts. *AIP Conference Proceedings*, *2223*. https://doi.org/10.1063/5.0000953

Pratiwi, R., Ibadurrohman, M., Dewi, E. L., Ratnawati, Yudianti, R., Husein, S., & Slamet. (2025). Development of CdS/TNTA nanocomposite to improve performance of simultaneous electrocoagulation-photocatalysis process for hydrogen production and ciprofloxacin elimination. *Materials Science for Energy Technologies*, *8*, 121–130. https://doi.org/10.1016/j.mset.2025.01.001

Pratiwi, R., Slamet, S., Chusniyah, D. A., & Yanti, W. (2022). SIMULTANEOUS ELECTROCOAGULATION-PHOTOCATALYTIC SCENARIO TO ENHANCE HYDROGEN PRODUCTION IN LIQUID WASTE TREATMENT: A BRIEF OVERVIEW. *Indonesian Journal of Urban and Environmental Technology*, *5*(3), 240–265. https://doi.org/10.25105/urbanenvirotech.v5i3.14447

Riyadh Atta, M., Shima Shaharun, M., Maksudur Rahman Khan, M., Abdullah, B., Fadhl Al-Mahmodi, A., Diyan Mohd Ridzuan, N., Devi Munusamy, T., & Jun Wei, L. (2023). Enhancing the photo-electrocatalytic properties of g-C3N4 by boron doping and ZIF-8 hybridization. *Inorganic Chemistry Communications*, *148*. https://doi.org/10.1016/j.inoche.2022.110235

Roy, A., & Pramanik, S. (2024). A review of the hydrogen fuel path to emission reduction in the surface transport industry. In *International Journal of Hydrogen Energy* (Vol. 49, pp. 792–821). Elsevier Ltd. https://doi.org/10.1016/j.ijhydene.2023.07.010

Saddique, Z., Imran, M., Javaid, A., Latif, S., Hussain, N., Kowal, P., & Boczkaj, G. (2023). Band engineering of BiOBr based materials for photocatalytic wastewater treatment via advanced oxidation processes (AOPs) – A review. In *Water Resources and Industry* (Vol. 29). Elsevier B.V. https://doi.org/10.1016/j.wri.2023.100211

Salman, R. H., & Abbar, A. H. (2023). Optimization of a combined electrocoagulation-electro-oxidation process for the treatment of Al-Basra Majnoon Oil field wastewater: Adopting a new strategy. *Chemical Engineering and Processing - Process Intensification*, *183*. https://doi.org/10.1016/j.cep.2022.109227

Song, M., Li, M., Li, H., Wang, P., Wu, Y., & Li, L. (2023). Novel through-holes g-C3N4/BiOBr S-scheme heterojunction: Charge relocation mechanism and DFT insights. *Surfaces and Interfaces*, *41*. https://doi.org/10.1016/j.surfin.2023.103227

Surjo, P., Pratiwi, R., Ratnawati, Yudianti, R., Dewi, E. L., & Slamet. (2024). Highly efficient CuO-doped titania nanotube arrays in photocatalysis-electrocoagulation process for bacterial disinfection. *Case Studies in Chemical and Environmental Engineering*, *9*. https://doi.org/10.1016/j.cscee.2024.100742

Tieng, S., Kanaev, A., & Chhor, K. (2011). New homogeneously doped Fe(III)-TiO2 photocatalyst for gaseous pollutant degradation. *Applied Catalysis A: General*, *399*(1–2), 191–197. https://doi.org/10.1016/j.apcata.2011.03.056

Wu, J., Xie, Y., Ling, Y., Dong, Y., Li, J., Li, S., & Zhao, J. (2019). Synthesis of Flower-Like g-C3N4/BiOBr and Enhancement of the Activity for the Degradation of Bisphenol A Under Visible Light Irradiation. *Frontiers in Chemistry*, *7*. https://doi.org/10.3389/fchem.2019.00649

Yang, L., Liang, L., Wang, L., Zhu, J., Gao, S., & Xia, X. (2019). Accelerated photocatalytic oxidation of carbamazepine by a novel 3D hierarchical protonated g-C 3 N 4 /BiOBr heterojunction: Performance and mechanism. *Applied Surface Science*, *473*, 527–539. https://doi.org/10.1016/j.apsusc.2018.12.180

Yuan, Y., Garg, S., Wang, Y., Li, W., Chen, G., Gao, M., Zhong, J., Wang, J., & Waite, T. D. (2022). Influence of salinity on the heterogeneous catalytic ozonation process: Implications to treatment of high salinity wastewater. *Journal of Hazardous Materials*, *423*. https://doi.org/10.1016/j.jhazmat.2021.127255

Yusuf, M., Rosha, P., Qureshi, F., Ali, F. M., & Ibrahim, H. (2025). Recent avenues in the photocatalytic splitting of water for eco-friendly hydrogen production. In *Sustainable Materials and Technologies* (Vol. 43). Elsevier B.V. https://doi.org/10.1016/j.susmat.2025.e01332

Zhang, B., Liu, Y., Zhou, K., Zhu, H., Gu, D., Ge, W., Gan, Y., & Hao, J. (2021). *Constructing BiOBr/g-C3N4/Bi2O2CO3 Z-Scheme Photocatalyst With Enhanced Photocatalytic Activity*. https://doi.org/10.21203/rs.3.rs-309897/v1

Zhang, L., Jia, C., Bai, F., Wang, W., An, S., Zhao, K., Li, Z., Li, J., & Sun, H. (2024). A comprehensive review of the promising clean energy carrier: Hydrogen production, transportation, storage, and utilization (HPTSU) technologies. *Fuel*, *355*. https://doi.org/10.1016/j.fuel.2023.129455

Zhang, X., Li, W., Hu, L., Gao, M., & Feng, J. (2024). A Tight-Connection g-C_3N_4/BiOBr (001) S-Scheme Heterojunction Photocatalyst for Boosting Photocatalytic Degradation of Organic Pollutants. *Nanomaterials*, *14*(13). https://doi.org/10.3390/nano14131071

Zuluaga, S., Liu, L. H., Shafiq, N., Rupich, S. M., Veyan, J. F., Chabal, Y. J., & Thonhauser, T. (2015). Structural band-gap tuning in g-C_3N_4. *Physical Chemistry Chemical Physics*, *17*(2), 957–962. https://doi.org/10.1039/c4cp05164e